Journal of Power Sources 196 (2011) 6299–6304

Contents lists available at ScienceDirect

Journal of Power Sources

journal homepage: www.elsevier.com/locate/jpowsour

Methane-fueled thin film micro-solid oxide fuel cells with nanoporous palladium anodes

Bo-Kuai Lai*, Kian Kerman, Shriram Ramanathan

Harvard School of Engineering and Applied Sciences, Harvard University, Cambridge, MA 02138, USA

ARTICLE INFO

Article history:
Received 10 February 2011
Received in revised form 28 March 2011
Accepted 29 March 2011
Available online 6 April 2011

Keywords:
Methane
Hydrocarbon
Palladium
Anode
Thin film
Solid oxide fuel cell

ABSTRACT

Methane-fueled thin film micro-solid oxide fuel cells (μSOFCs) based on palladium (Pd) anodes are discussed in this article. The μSOFCs are composed of porous platinum (Pt) cathodes, 8 mol.% yttria-stabilized zirconia (YSZ) ultrathin electrolytes, and Pd anodes – specifically, a Pt/YSZ/Pd heterostructure synthesized by physical vapor deposition. The Pt/YSZ/Pd μSOFCs exhibit a power density of 385 mW cm^{-2} and an open circuit voltage of 0.77 V at 550 °C. A detailed study on synthesis, microstructure and functional properties of the nanoporous Pd films is presented. Possible anodic methane reactions, carbon deposition on Pd anodes, and carbon suppression approaches are discussed. The results are of potential relevance to advancing low temperature micro-fuel cell technology using hydrocarbon fuels.

1. Introduction

Fuel flexibility is considered to be a key advantage of solid oxide fuel cells (SOFCs) [1,2]. In addition to hydrogen (H_2), hydrocarbons (C_nH_{2n+2}), natural gas, biogases, biofuels, and military logistic fuels may also be used to operate SOFCs [3]. The use of pure hydrogen is challenging to implement on a large scale. Moreover, majority of H_2 produced is via steam reforming of methane (CH_4), increasing the cost and lowering the overall energy efficiency of H_2 fuels. Hydrocarbons (C_nH_{2n+2}) and natural gas are widely available and some biofuels such as butanol and Fischer–Tropsch fuels could potentially be distributed via existing automobile gasoline infrastructure [4]. As a result, SOFCs operated by these H_2-alternative fuels are highly desirable and have emerged as a significant research topic.

Among H_2-alternative fuels, hydrocarbons such as methane and n-butane receive substantial research attention and have been successfully demonstrated to operate SOFCs [1,5–10]. For example, a methane-fueled SOFC, which used ~1 mm thick Ni-YSZ anodes, reported by Lin et al. [10] exhibited a peak power density (P_{max}) of 200 mW cm^{-2} and an open circuit voltage (OCV) of 1.05 V at 600 °C. A critical challenge in methane-fueled SOFCs is lowering their operating temperatures while maintaining acceptable performance. In this report, we will address this challenge based on the high-performance μSOFC platform that has been developed in recent years [11–16]. Such μSOFCs have been demonstrated to achieve >1000 mW cm^{-2} power density at 500 °C [17] and 861 mW cm^{-2} at 450 °C [18], in part due to high flux of electron-generating O^{2-} transport through ultrathin electrolytes. As discussed in Ref. [19], high O^{2-} flux towards the anode of direct hydrocarbon-fueled μSOFCs is critical to minimize carbon deposition (coking).

We chose methane (CH_4) as the fuel in this study because it is among the most widely studied hydrocarbons. It has the following advantages over other higher hydrocarbons: (i) the smallest carbon footprint due to the lowest C/H_2 ratio; (ii) it is abundant and can be produced from oil drilling, coal mining, and biomass decomposition; (iii) it constitutes ~85% of natural gas and more than 50% of typical biogases, both of which are very promising H_2-alternative fuels for SOFCs. Moreover, methane gas is used to produce methanol [20], which is an important liquid fuel. Therefore, methane is a very appealing H_2-alternative fuel for SOFCs.

Since methane is a stable hydrocarbon [21], a highly active anode catalyst towards CH_4 oxidation or cracking is critical to realize methane-fueled SOFCs at low temperatures. Catalytic systems for complete oxidation ($CH_4 + 2O_2 \rightarrow CO_2 + 2H_2O$, methane combustion) [22], partial oxidation ($2CH_4 + O_2 \rightarrow 2CO + 4H_2$) [23], steam reforming ($CH_4 + H_2O \rightarrow CO + 3H_2$) [20], and catalytic cracking ($CH_4 \rightarrow C + 2H_2$) [20] of methane for H_2 or synthesis gas production have been studied. Most studies show that Pd supported by redox-capable oxides [24–27] exhibits excellent low temperature catalytic activity in the aforementioned methane reactions; the redox-capable oxides include ceria [24,28], zirconia [29–31], and ceria-zirconia [32]. For example, Pd/zirconia systems can completely convert methane via complete oxidation of methane at $T < 500$ °C [31] and convert 90% of methane to synthesis gas via

* Corresponding author. Tel.: +1 617 497 4632; fax: +1 617 497 4627.
E-mail addresses: bokuai.lai@gmail.com, blai@seas.harvard.edu (B.-K. Lai).

0378-7753/$ – see front matter © 2011 Elsevier B.V. All rights reserved.
doi:10.1016/j.jpowsour.2011.03.093

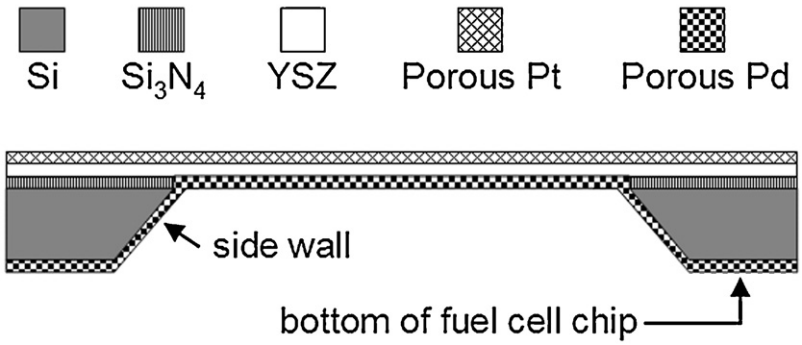

Fig. 1. A schematic cross-sectional view of a μSOFC. Pd thin films cover whole anode side of the μSOFC, including fuel cell anode, side walls of etched Si wells, and the bottom of fuel cells chips.

partial oxidation of methane at $T = 630\,^{\circ}C$ [21]; while in contrast, without any catalyst, temperature has to reach ~800 °C to thermally decompose 95% of methane ($CH_4 \rightarrow C + 2H_2$) [21].

It is worth noting that, when exposed to ambient air ($pO_2 = 0.21$ atm), Pd bulk oxidizes to PdO in 300–400 °C range with a change in unit cell volume and PdO is stable in ambient air up to ~700 °C. The active lattice and electronic structures of Pd and PdO in this temperature range is essential to understand the behavior of complete oxidation of methane, for which methane conversion typically starts to take place at 300 °C and achieves a >90% rate at temperatures as low as 400 °C [31]. It is generally accepted that the presence of PdO on Pd particles or films is essential to achieve a high catalytic reactivity towards methane [22,33,34].

The fact that both ceria and zirconia are typical SOFC electrolytes or part of electrode matrices and the temperatures for high conversion rate is in the range of interest to μSOFCs, as well as good thermal expansion coefficient matching between Pd (~$11.5 \times 10^{-6}\,K^{-1}$) and YSZ (~$10.1 \times 10^{-6}\,K^{-1}$) [35,36], indicate Pd would be an appealing anode material to explore for methane-fueled μSOFCs. Although there have been attempts to incorporate Pd as anode materials in conventional SOFCs [37–41], to the best of authors' knowledge, this is the first report on such efforts with thin film μSOFCs operated in methane.

Our objective is to explore high-performance methane-fueled μSOFCs based on Pd anodes. The electrolytes and cathodes are thin film YSZ and Pt, respectively. Since Pd has never been discussed before in thin film μSOFCs, emphasis topics in this paper are on the synthesis and understanding of Pd thin films and on the performance of methane-fueled μSOFCs based on Pd anodes. Our results show that a peak power density of 385 mW cm^{-2} and an open circuit voltage of 0.77 eV can be achieved at 550 °C. Carbon deposition, a concern for hydrocarbon-fueled SOFCs, was observed and will be discussed.

2. Experimental details

Deposition of 8 mol.% yttria-doped zirconia (YSZ) films were performed in 5 mTorr Ar plasma and at 100 W target power by radio-frequency sputtering from a stoichiometric target. Both platinum (Pt) and palladium (Pd) thin films were deposited by direct-current sputtering in 75 mTorr Ar and at 250 W target power. Substrates were not heated during these depositions. Nominal deposition rates of as-deposited YSZ, Pt, and Pd thin films on single crystalline (1 0 0) YSZ (sc-YSZ) substrates were ~1.5, ~5.4, and ~3.3 nm min^{-1}, respectively, estimated from X-ray reflectivity. The same deposition chamber was used to anneal Pd in vacuum, with pressures lower than 5×10^{-6} mTorr. Grazing incidence (at 1° omega) and theta – 2 theta ($\theta - 2\theta$) X-ray diffraction (XRD) were performed with a Scintag 2000 diffractometer using Cu K_α radiation. Surface morphology was investigated by Carl Zeiss Ultra 55 field emission scanning electron microscopy (SEM). Lateral electrical conductivity of as-deposited Pd thin films on sc-YSZ substrates at room temperature were measured by a Creative Design Engineering ResMap 168 four-point probe resistivity mapping system. High temperature lateral electrical conductivity measurement of as-deposited Pd thin films on sc-YSZ substrates were performed using the same electrode configuration and procedure detailed in Ref. [42] and fuel cell testing system described in Ref. [16].

μSOFC membranes were fabricated on Si_3N_4-coated Si chips with dimensions of 10 mm × 10 mm × 0.5 mm. The fabrication procedure was as follows: (i) Si_3N_4 thin films were patterned by photolithography and then removed by reactive ion etching (RIE); (ii) 30% KOH was used to etch through Si, forming Si wells, to release free standing Si_3N_4 thin films from Si; (iii) YSZ and then Pt were deposited onto the cathode side; (iv) RIE was used to remove Si_3N_4 on the anode side to release Pt/YSZ thin films; (v) Pd was deposited onto the anode side, yielding Pt/YSZ/Pd μSOFC membranes. The width of square μSOFC membranes was in 150–160 μm range, as measured by SEM. Fig. 1 shows a schematic cross-sectional view of a μSOFC. Note that side walls of etched Si wells and the bottom of fuel cell chips were also coated with Pd during deposition of Pd anode. Detailed fabrication considerations and procedures have been discussed in Refs. [43,44]. During fuel cell measurements, humidified pure CH_4 at a flow rate of 200 ml min^{-1} or 5% H_2 forming gases at a flow rates of 100 ml min^{-1} were fed to the anodes on the bottom of the chips while the cathodes were exposed to laboratory air.

3. Results and discussion

3.1. Pd thin films

To synthesize Pd thin films with suitable porosity for fuel cell operation, Pd thin films of different thicknesses were deposited on sc-YSZ substrates at 75 mTorr, which is a similar pressure range as porous Pt anode deposition in previous works [43,44]. Fig. 2(a) shows a XRD pattern of a 66 nm thick as-deposited Pd thin film. Powder diffraction of polycrystalline Pd from JCPDS 03-065-2867 is displayed on the bottom of Fig. 2; in which Pd (1 1 1) and (2 0 0) peaks are located at 40.11° and 46.65° 2θ, respectively, and intensity ratio of Pd (1 1 1) to (2 0 0) peaks is ~0.45. Referring to JCPDS 03-065-2867, as-deposited Pd thin films were in cubic phase with a preferred orientation of (1 1 1). The intensity ratio of Pd (1 1 1) to (2 0 0) peaks in Fig. 2(a) is ~0.21. The relatively large full width at half maximum (FWHM), ~0.9°, of (1 1 1) peaks indicated nanocrystallinity of as-deposited Pd thin films. Room temperature electrical conductivity of the as-deposited Pd thin film was in $23–28 \times 10^3$ S cm^{-1} range. In contrast, conductivity of bulk Pd is ~100×10^3 S cm^{-1}. The difference is due to nanocrystalline mor-

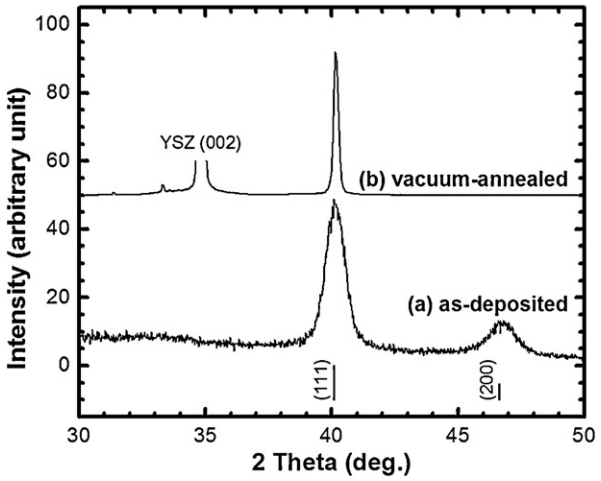

Fig. 2. XRD of 66 nm thick Pd thin films that were (a) as-deposited and (b) annealed in vacuum at 550 °C for 1 h. The substrates were single crystalline YSZ (1 0 0). Position and relative intensity of Pd (1 1 1) and (2 0 0) XRD peaks (JCPDS 03-065-2867) are also plotted. (a) was taken at a grazing incidence angle of 1° omega; while (b) was taken using $\theta - 2\theta$ scan.

phology [45] and loosely packed Pd nano-grains. As seen in Fig. 3(a), the nominal grain size for a 66 nm thick as-deposited Pd thin film is 35 ± 5 nm. After annealing in vacuum at 550 °C for 1 h (referred to as vacuum-annealed hence-forth), three changes were noted. First, Pd thin films became (1 1 1)-textured. The XRD pattern in Fig. 2 for an annealed 66 nm thick Pd thin film was obtained using $\theta - 2\theta$ scan. For better comparison of Pd XRD peaks, YSZ (0 0 2) peak at 35.87° 2θ from Cu K_α radiation in Fig. 2 was truncated. A small peak at ~34° 2θ was YSZ (0 0 2) from Cu $K_{\beta 1}$ radiation. Similar orientation trends have also been observed for Pt thin films on sc-YSZ (1 0 0) substrates [46,47] and the lattice misfit is accommodated by twinning of Pt domains. Since Pd and Pt are both cubic and have similar lattice constants (Pd: 0.389 nm; Pt: 0.392 nm) and several other physical properties, it is possible that the rationale for explaining behavior of Pt may be extended to Pd.

Second, significant microstructural changes and grain growth was observed (see Fig. 3). The grain size in vacuum-annealed Pd thin films varied from tens to hundreds of nm and their fish scale-like grain morphology is similar to the (1 1 1)-textured Pt thin films on sc-YSZ (1 0 0) substrates [46]. The larger grain size was also manifested in the FWHM of Pd (1 1 1) peak shown in Fig. 2, which changes from 0.9° to 0.2° after the annealing. The grain size increase suggest that mass transport of Pd in reducing environment is active at $T < 550$ °C. Third, there was an increase in electrical conductivity of Pd thin films after annealing, as seen in Fig. 4. For Pd thin films thicker than 56 nm, the conductivity increased by three fold and reached up to 75% of bulk (100×10^3 S cm^{-1}) after annealing. This is attributed to the grain growth, which reduces grain boundary electron scattering [45], and denser microstructures. As demonstrated in Fig. 3(c), the thickness dependence of electrical conductivity for thinner Pd thin films is probably related to their nanoporous morphology and different granular structures.

3.2. μSOFCs with Pd anodes

It is crucial to control the thickness of Pd anodes. If an anode film is too thin, microstructure will be unstable at operating temperatures and hence performance will degrade quickly; if an anode film is too thick, there will be no porosity to facilitate anodic reaction and hence the fuel cell will have no performance at all. The conductivity (Fig. 4) and SEM (Fig. 3) results suggest that, when thickness is less than ~56 nm, Pd thin films possess slightly porous microstructure

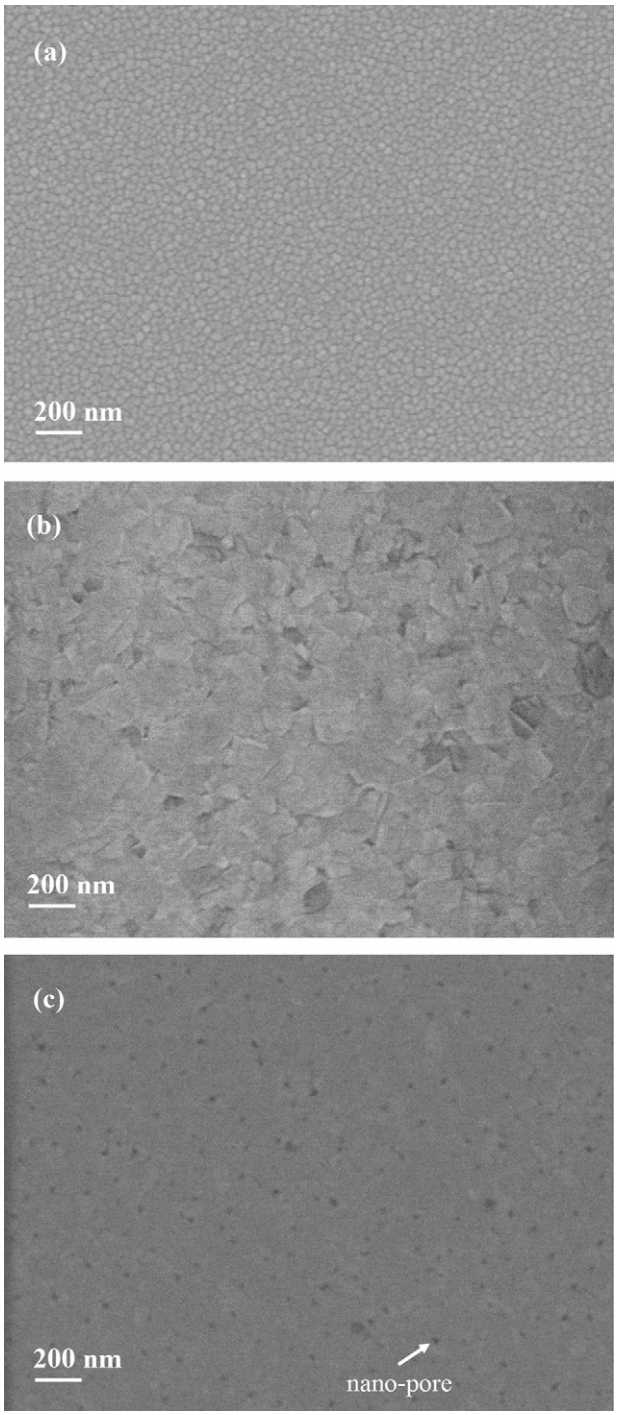

Fig. 3. SEM images of 66 nm thick as-deposited Pd thin films that were (a) as-deposited and (b) annealed annealing in vacuum at 550 °C for 1 h. (c) SEM image of a 26 nm thick Pd thin film after annealing in vacuum at 550 °C for 1 h. The substrates were single crystalline YSZ (1 0 0).

and good electrical conductivity in a high temperature reducing environment. Therefore, 50 nm was chosen as the thickness for Pd anode in the fuel cell studies. Fig. 5(a) shows surface morphology of a 50 nm thick as-deposited Pd anode on the bottom of an etched Si well. As seen, the Pd anode was composed of discrete Pd clusters, which is similar to the optimum surface morphology of Pt anode in the high performance μSOFCs reported in Ref. [17]. Such morphology, however, is different from the packed, well-connected Pd grains seen in the 66 nm thick Pd thin films on sc-YSZ substrates (Fig. 3(a)). The droplet-like morphology might be related to tem-

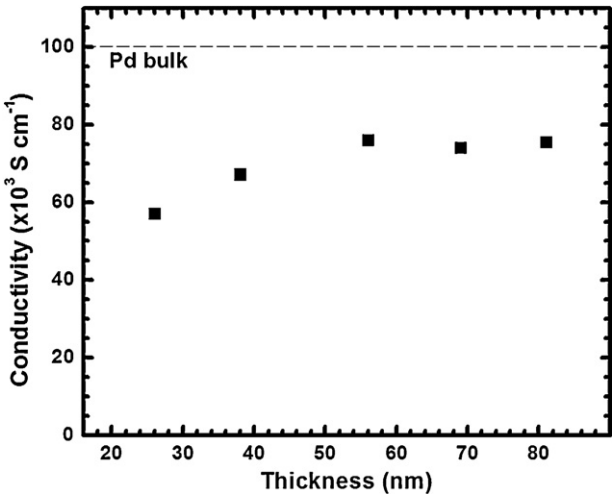

Fig. 4. Room temperature electrical conductivity for Pd thin films of varying thicknesses annealed in vacuum at 550 °C for 1 h. A horizontal dash line represents the typical conductivity (100×10^3 S cm^{-1}) of bulk Pd.

perature and morphology of growth surface being different from that of single crystal substrates.

μSOFCs with 70 nm thick porous Pt cathodes, 100 nm thick dense YSZ electrolyte, and 50 nm thick Pd anodes (referred to as Pt/YSZ/Pd μSOFCs) were fabricated following the procedure

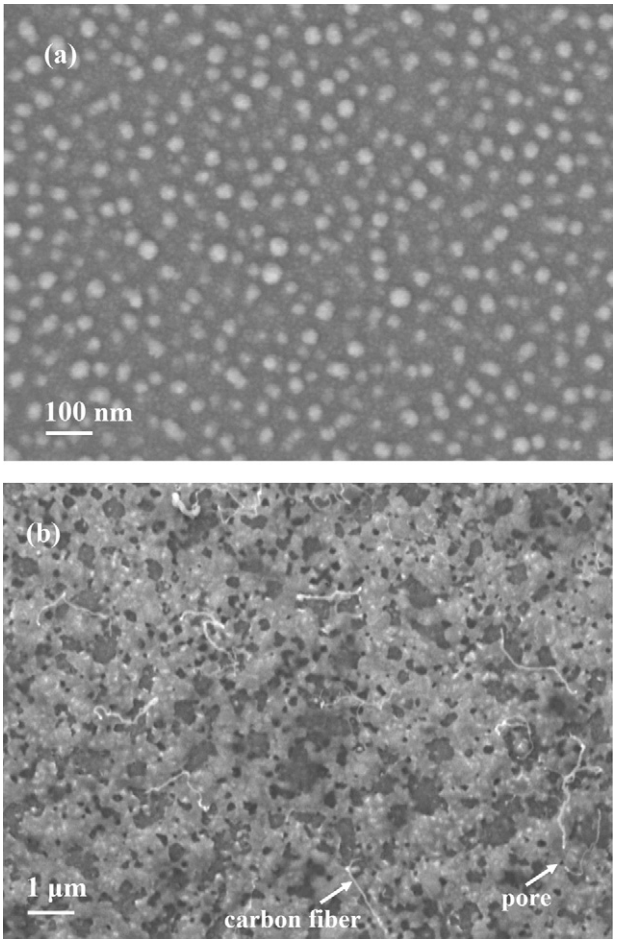

Fig. 5. SEM images of 50 nm thick Pd anodes on a μSOFC membrane (a) before and (b) after fuel cell testing. Carbon fibers are indicated by white arrows. Pores that could be the roots of oxidized carbon fibers are also indicated by white arrows.

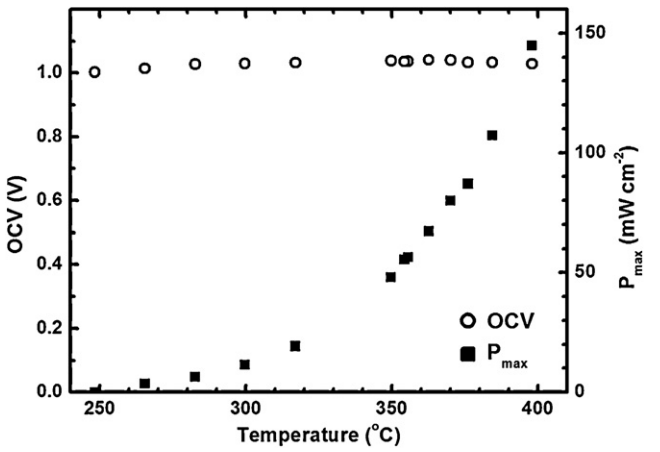

Fig. 6. Open circuit voltage (OCV, ○) and peak power density (P_{max}, ■) as a function temperature for a H_2-fueled Pt/YSZ/Pd μSOFC.

described in Ref. [44]. To ensure appropriate choice of Pd thickness, a Pt/YSZ/Pd μSOFC was first tested up to 400 °C using H_2 fuel. Fig. 6 shows its open circuit voltage (OCV) and peak power density (P_{max}) as a function of temperature. As seen, OCV was stable and higher than 1.0 V in 250–400 °C range. At 400 °C, the H_2-fueled Pt/YSZ/Pd μSOFC exhibited P_{max} = 145 mW cm^{-2} and OCV = 1.03 V. Such performance is ~50% of that of recently reported H_2-fueled Pt/YSZ/Pt μSOFCs [17], which exhibited P_{max} = 300 mW cm^{-2} and OCV = 1.0 V at 400 °C. The result further indicated that 50 nm is a suitable thickness for Pd anodes and its corresponding structure would evolve into a suitable porous morphology at temperature as low as 250 °C.

An identical Pt/YSZ/Pd μSOFC was then tested using CH_4 fuel. Fig. 7(a) shows its temperature-dependent OCV and P_{max}. Methane was supplied before the fuel cell was heated for testing and until the tested μSOFC cooled down below ~100 °C. As seen in Fig. 7(a), OCV stabilized at 0.82 ± 0.02 V in 380–530 °C range. P_{max} and OCV reached 200 mW cm^{-2} and 0.84 V, respectively, at 500 °C and 385 mW cm^{-2} and 0.77 V, respectively, at 550 °C. Voltage and power density as a function of current density at 440 °C, 500 °C, and 550 °C are plotted in Fig. 7(b); when temperature increased from 440 °C to 500 °C, ohmic loss decreased apparently. Fig. 5(b) shows surface morphology of Pd anode after 5 h of fuel cell testing. As seen, a very small amount of carbon deposition in the form of fibers was observed. Small pores might be the roots of carbon fibers, which were oxidized ($C + 2O^{2-} \rightarrow CO_2$) and removed from the anode at high temperatures during testing when supply of oxygen ions is abundant. We also observed carbon fibers on the side walls of etched Si wells, which were also coated with Pd during anode deposition. Carbon deposition on non-reactive regions of SOFC anodes has also been reported in the literature [48].

The observed carbon deposition on anode surface and side walls is likely formed via catalytic cracking of methane ($CH_4 \rightarrow C + 2H_2$) on Pd anodes [6]. Note that complete oxidation [1,6] and partial oxidation [49] of methane are unlikely the dominant anodic reactions because the required critical O^{2-}/CH_4 ratio [10] of ~0.5 and ~1.5, respectively, for the reaction to dominate. These ratios are much higher than our testing conditions-namely, oversupply of CH_4 and low flux of O^{2-} at low temperatures. The methane cracking products (C and H_2) would then react with O^{2-} via carbon oxidation ($C + O^{2-} \rightarrow CO + 2e^-$) and hydrogen oxidation ($H_2 + O^{2-} \rightarrow H_2O + 2e^-$) reactions and produce electrons to external circuits. The corresponding ideal Nernst potentials with these two reactions at 450 °C are ~1.05 and ~1.15 V [10,50], both are higher than the measured OCV (0.82 ± 0.02 V in 380–530 °C range). We speculate that the discrepancy between measured and ideal

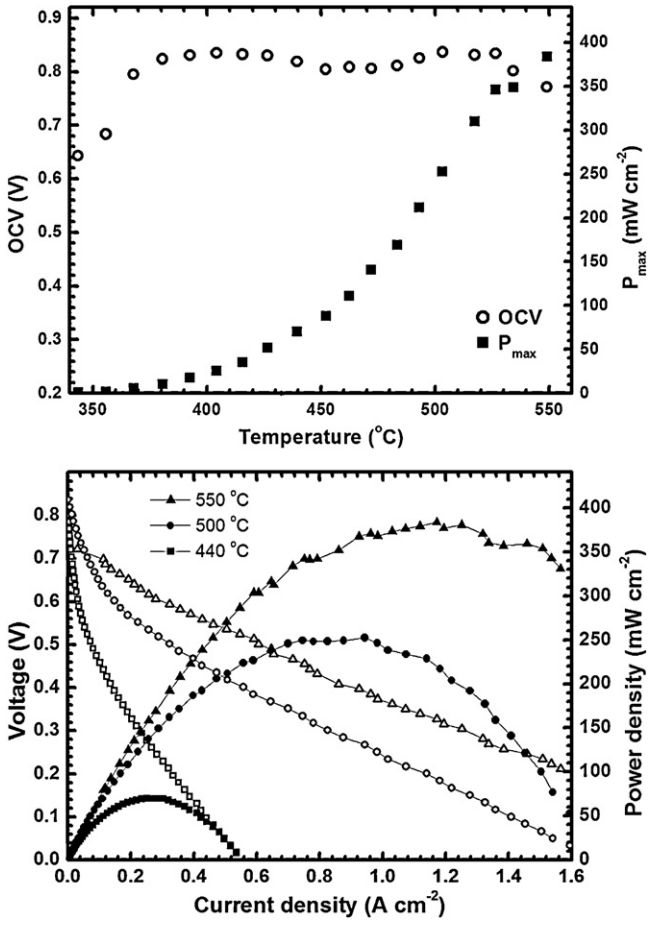

Fig. 7. (a) Open circuit voltage (OCV, ○) and peak power density (P_{max}, ■) as a function temperature for a CH_4-fueled Pt/YSZ/Pd μSOFC. (b) Voltage (open symbols) and power density (solid symbols) as a function of current density at 440 °C (square symbols), 500 °C (circular symbols), and 550 °C (triangular symbols) for a CH_4-fueled Pt/YSZ/Pd μSOFC.

OCV is related to carbon deposition. The carbon deposition on the Pd anode may block or impede hydrogen oxidation. The observed carbon deposition, which might delaminate Pd films [49], on the side walls of etched Si wells or on the bottom of nanoporous Pd-covered testing Si chips could also lead to voltage loss. Note that carbon deposition depends on the balance of O^{2-} flux and cracking efficiency, both increase with temperature, and could occur over a wide temperature range. Since cracking efficiency is higher at high temperatures, carbon deposition could rapidly degrade fuel cells if sufficient O^{2-} flux is not supplied at high temperatures [10,19,51]. Besides methane cracking, CO disproportionation ($2CO \rightarrow C + CO_2$, $\Delta H_{298} = -172.4\,kJ\,mol^{-1}$), CO reduction reaction ($CO + H_2 \rightarrow C + H_2O$, $\Delta H_{298} = -132.2\,kJ\,mol^{-1}$), and CO_2 reduction reaction ($CO_2 + 2H_2 \rightarrow C + 2H_2O$, $\Delta H_{298} = -90.15\,kJ\,mol^{-1}$) could also lead to carbon deposition [19]. These reactions are exothermic and preferred at low temperatures.

To minimize carbon deposition, several approaches have been reported and could likely be implemented to further improve the methane-fueled μSOFCs reported here. First, ceria-based anodes have been demonstrated to suppress carbon deposition [1,6,7]. Second, increased partial pressure of H_2O could suppress carbon-generating CO and CO_2 reduction reactions or remove carbon via $C + H_2O \rightarrow CO + H_2$, $\Delta H_{298} = 131.19\,kJ\,mol^{-1}$, at high temperatures, as suggested in Ref. [52]. Third, precise control of CH_4 supply to maintain a O^{2-}/CH_4 ratio of ~1.0 has been demonstrated to convert over 90% of CH_4 into synthesis gas with little carbon deposition via methane cracking [53].

4. Conclusions

Functional methane-fueled thin film μSOFCs based on nanoporous Pd anode, YSZ electrolyte, and Pt cathode has been demonstrated. Nanocrystalline porous Pd thin films with good electrical conduction properties were synthesized by performing sputtering at high pressures and controlling their thicknesses in the vicinity of nominal grain size. The Pt/YSZ/Pd μSOFCs exhibit a peak power density of 385 mW cm^{-2} and an open circuit voltage of 0.77 V at 550 °C. Carbon deposition was observed and approaches to manage it have been discussed. The results presented in this manuscript could be relevant towards further advancing low temperature fuel-flexible solid oxide fuel cells using thin film components.

Acknowledgments

We are grateful to National Science Foundation Grant CCF-0926148 for financial support. The authors acknowledge Suhare Adam for assistance with scanning electron microscopy, Yuto Takagi (Harvard) and Prof. Steve McIntosh (Lehigh University) for valuable discussions.

References

[1] S. Park, J.M. Vohs, R.J. Gorte, Nature 404 (2000) 265–267.
[2] B.C.H. Steele, A. Heinzel, Nature 414 (2001) 345–352.
[3] B.C.H. Steele, Nature 400 (1999) 619–621.
[4] T.L. Richard, Science 329 (2010) 793–796.
[5] T. Hibino, A. Hashimoto, T. Inoue, J.-I. Tokuno, S.-I. Yoshida, M. Sano, Science 288 (2000) 2031–2033.
[6] M. Mogenson, K. Kammer, Annu. Rev. Mater. Res. 33 (2003) 321–331.
[7] E.P. Murray, T. Tsai, S.A. Barnett, Nature 400 (1999) 649–651.
[8] S. McIntosh, R.J. Gorte, Chem. Rev. 104 (2004) 4845–4865.
[9] Y.-H. Huang, R.I. Dass, Z.-L. Xing, J.B. Goodenough, Science 312 (2006) 254–257.
[10] Y. Lin, Z. Zhan, J. Liu, S.A. Barnett, J. Power Sources 176 (2005) 1827–1835.
[11] A.F. Jankowski, J.P. Hayes, R.T. Graff, J.D. Morse, Mat. Res. Soc. Symp. Proc. 730 (2002), V4.2.1.
[12] X. Chen, N.J. Wu, L. Smith, A. Ignatiev, Appl. Phys. Lett. 84 (2004) 2700–2702.
[13] H. Huang, M. Nakamura, P.C. Su, R. Fasching, Y. Saito, F.B. Prinz, J. Electrochem. Soc. 154 (2007) B20–B24.
[14] A. Bieberle-Hutter, D. Beckel, A. Infortuna, U.P. Muecke, J.L.M. Rupp, L.J. Gauckler, S. Rey-Mermet, P. Muralt, N.R. Bieri, N. Hotz, M.J. Stutz, D. Poulikakos, P. Heeb, P. Muller, A. Bernard, R. Gmur, T. Hocker, J. Power Sources 177 (2008) 123–130.
[15] A. Ignatiev, X. Chen, N.J. Wu, Z.G. Lu, L. Smith, Dalton Trans. (2008) 5501–5506.
[16] A.C. Johnson, B.-K. Lai, H. Xiong, S. Ramanathan, J. Power Sources 186 (2009) 252–260.
[17] K. Kerman, B.-K. Lai, S. Ramanathan, J. Power Sources 196 (2011) 2608–2614.
[18] P.-C. Su, C.-C. Chao, J.H. Shim, R. Fasching, F.B. Prinz, Nano Lett. 8 (2008) 2289–2292.
[19] W. Wang, Y. Cao, Int. J. Hydrogen Energy 35 (2010) 13280–13289.
[20] J.N. Armor, Appl. Catal. A: Gen. 176 (1999) 159–176.
[21] M.M. Halmann, M. Steinberg, Greenhouse Gas Carbon Dioxide Mitigation: Science and Technology, CRC Press, 1998, pp. 221–252.
[22] P. Gelin, M. Primet, Appl. Catal. B: Environ. 39 (2002) 1–37.
[23] A.T. Ashcroft, A.K. Cheetham, M.L.H. Green, P.D.F. Vernon, Nature 351 (1991) 225–226.
[24] X. Wang, R.J. Gorte, Catal. Lett. 73 (2001) 15–19.
[25] H. Zhang, J. Gromek, G.W. Fernando, S. Boorse, H.L. Marcus, J. Phase Equilib. 23 (2002) 246–248.
[26] T. Choudhary, S. Banerjee, V. Choudhary, Appl. Catal. A: Gen. 234 (2002) 1–23.
[27] L.S. Escandon, S. Ordonez, A. Vega, F.V. Díez, J. Hazard. Mater. 153 (2008) 742–750.
[28] R. Craciun, B. Shereck, R.J. Gorte, Catal. Lett. 51 (1998) 149–153.
[29] M.Y. Smirnov, G.W. Graham, Catal. Lett. 72 (2001) 39–44.
[30] S. Sharma, S. Hilaire, R.J. Gorte, Stud. Surf. Sci. Catal. 130 (2000) 677–682.
[31] S. Guerrero, P. Araya, E.E. Wolf, Appl. Catal. A: Gen. 298 (2006) 243–253.
[32] D. Ciuparu, L.D. Pfefferle, Appl. Catal. A: Gen. 218 (2001) 197–209.
[33] C.A. Muller, M. Maciejewski, R.A. Koeppel, A. Baiker, J. Catal. 166 (1997) 36–43.
[34] Y.-H. Chin, D.E. Resasco, Catalysis, The Royal Society of Chemistry, 1999, pp. 1–39.
[35] H. Hayashi, T. Saitou, N. Maruyama, H. Inaba, K. Kawamura, M. Mori, Solid State Ionics 176 (2005) 613–619.

[36] X. Lu, J. Zhu, Solid State Ionics 178 (2007) 1467–1475.
[37] S. Sengodan, H.J. Yeo, J.Y. Shin, G. Kim, J. Power Sources 196 (2011) 3083–3088.
[38] D.M. Bierschenk, E. Potter-Nelson, C. Hoel, Y. Liao, L. Marks, K.R. Poeppelmeier, S.A. Barnett, J. Power Sources 196 (2011) 3089–3094.
[39] A. Babaei, L. Zhang, S.L. Tan, S.P. Jiang, Solid State Ionics 181 (2010) 1221–1228.
[40] S.P. Jiang, Y. Ye, T. He, S.B. Ho, J. Power Sources 185 (2008) 179–182.
[41] K. Asano, Y. Tominaga, Y. Mugikura, T. Watanabe, Solid State Ionics 181 (2010) 236–239.
[42] B.-K. Lai, K. Kerman, S. Ramanathan, J. Power Sources 195 (2010) 5185–5196.
[43] B.-K. Lai, H. Xiong, M. Tsuchiya, A.C. Johnson, S. Ramanathan, Fuel Cells 9 (2009) 699–710.
[44] B.-K. Lai, K. Kerman, S. Ramanathan, J. Power Sources 196 (2011) 1826–1832.
[45] T. Sun, B. Yao, A.P. Warren, K. Barmak, M.F. Toney, R.E. Peale, K.R. Coffey, Phys. Rev. B 81 (2000) 155454.
[46] G. Beck, H. Fischer, E. Mutoro, V. Srot, K.P.E. Tchernychova, M. Wuttig, M. Rühle, B. Luerßen, J. Janek, Solid State Ionics 178 (2007) 327–337.
[47] D. Hesse, S.K. Lee, U. Gösele, Phys. Status Solidi A 202 (2005) 2287–2298.
[48] A. Weber, B. Sauer, A.C. Muller, D. Herbstritt, E. Ivers-Tiffee, Solid State Ionics 152 (2002) 543–550.
[49] S. Hamakawa, M. Koizumi, K. Sato, J. Nakamura, T. Uchijima, K. Murata, T. Hayakawa, K. Takehira, Catal. Lett. 52 (1998) 191–197.
[50] J. Liu, S.A. Barnett, Solid State Ionics 158 (2003) 11–16.
[51] V. Antonucci, J. Power Sources 62 (1996) 95–99.
[52] M.R. Pillai, D.M. Bierschenk, S.A. Barnett, Catal. Lett. 121 (2008) 19–23.
[53] Z. Zhan, Y. Lin, M. Pillai, I. Kim, S.A. Barnett, J. Power Sources 161 (2006) 460–465.